Int. J. Electrochem. Sci., 10 **(2015)** 2487 - 2503

International Journal of
ELECTROCHEMICAL
SCIENCE
www.electrochemsci.org

Anode- Versus Cathode-Supported Solid Oxide Fuel Cell: Effect of Cell Design on the Stack Performance

Shichuan Su, Xiang Gao, Qiang Zhang, Wei Kong and Daifen Chen**

School of Energy and Power Engineering, Jiangsu University of Science and Technology, Zhenjiang 212003, China
*E-mail: wkong@just.edu.cn, dfchen@mail.ustc.edu.cn

Received: 24 November 2014 / *Accepted:* 22 December 2014 / *Published:* 19 January 2015

This paper investigates the effect of cell design on solid oxide fuel cells (SOFC) stack performance. Based on 3-dimensional numerical simulations, it is found that the performance of stack is strongly dependent on cell design. The average current density of the anode-supported SOFC (ASC) stack is only 5580 A m^{-2}, a reduction of 20.7% from the cathode-supported SOFC (CSC) stack of 7033 A m^{-2}. This can be explained that compared with CSC stack, thin cathode in ASC stack leads to the smaller effective reaction zone and the larger cathode ohmic losses. The discrepancy between the ASC stack and the CSC stack are examined by varying rib width, contact resistance and pitch width. The results show conclusively that with the optimal rib width, the performance of the CSC stack is much superior to that of the ASC stack for any practical contact resistance and pitch width. The analyses provided in this paper assist in understanding the effect of cell design on cell performance in the stack level and playing the full potential of the stack by optimizing the cell design.

Keywords: Solid oxide fuel cell; Anode-supported cell; cathode-supported cell; stack model; charge or gas transport

1. INTRODUCTION

As one of the common SOFC configurations, planar-type has attracted much more attention due to shorter current paths and higher power density over tubular-type design [1]. To date, two main types planar SOFC have been studied. They are electrolyte- and electrode-supported designs. For electrolyte-supported SOFC, high working temperature is required in order to reduce the electrolyte ohmic loss [2]. However, high working temperature is also a rigorous limit for materials of SOFC and decreases fuel cell lifetime and increases fabrication cost [1, 3-5]. For electrode-supported SOFC, electrolyte is very thin (for example, about 10 μm), which drastically reduces the electrolyte ohmic

loss. Thus electrode-supported SOFC can be operated at intermediate or low temperature and is preferred over electrolyte-supported design [6].

Much recent effort for the electrode-supported SOFC is mainly based on the anode-supported SOFC (ASC) [7-11]. Noh et al. showed that the cell performance was improved by a factor of 1.6 by the optimization of the current collection configuration of ASC [12]. Author's previous study systematically examined the influence of the rib width on the stack-cell performance and revealed that the optimal rib width of anode is quite different from that of cathode for ASC[13]. Park et al investigated the effect of the anode functional layer thickness on the performance of ASC[14]. Lim et al. studied the degradation mechanism of ASC. The results indicated that the increase of the ohmic resistance is the main cause leading to the cell degradation [15].

Comparatively, there has been little attention paid to the cathode-supported SOFC (CSC), though CSC shows various advantages over ASC such as using the low-cost cathode supporting material strontium-doped lanthanum manganese, relatively thin anode preventing the depositing carbon when operating on hydrocarbon fuels and also providing benefits in terms of tolerance to volume contraction/expansion resulting from the accidental anode redox cycles [6, 16-19]. This can be highly attributed to the fabrication difficulty of the CSC. For example, a relatively high sintering temperature may lead to the chemical reactions between cathode and electrolyte. However, the electrolyte will not be dense if sintered at a low temperature[18].

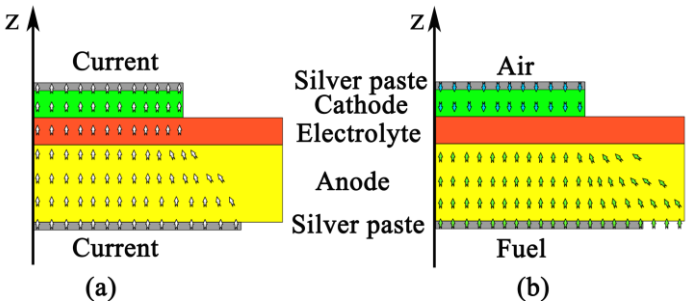

Figure 1. Schematic representation of charge and gases transport processes in the button cell.

For the button cell, silver paste is often used as current collector [20, 21]. Therefore, the charge or gases transport processes in the parallel electrode surface direction can be neglected, as shown in Fig.1. The ohmic and concentration losses of electrodes are mainly due to the transport processes in the vertical electrode surface direction. As we all know, anode conductivity is about 6 times higher than the cathode conductivity. Hydrogen diffusion coefficient is also larger than oxygen diffusion coefficient. Thus the performance of the ASC is superior to that of the CSC for the button cell [1, 22, 23].

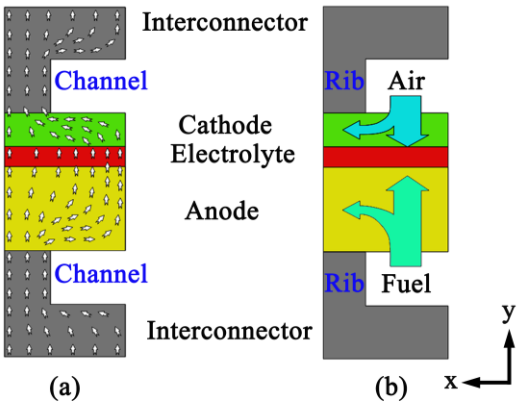

Figure 2. Schematic representation of charge and gases transport processes in the stack.

For the stack, the channels in interconnector are used to carry the fuel and air flows and the ribs collect current, which separate and define the channels, as shown in Fig. 2. The width of the ribs or the channels is commonly about several millimeters [13, 24]. The charge and gases transport paths of the stack in the parallel electrode surface direction is no less than that in the vertical electrode surface direction. Therefore, at least, the ohmic and concentration losses of electrodes in the parallel electrode surface direction are the same important as those in the vertical electrode surface direction. Thick electrode layer is benefit for reducing the ohmic and concentration losses in the parallel electrode surface direction due to increasing the cross section of the charge and gases transport paths. On the other hand, thick electrode layer hinders the charge and gases transport in the vertical electrode surface direction because of elongating the charge and gases transport path. Thus it is difficult to judge whether the performance of the ASC stack is better than that of the CSC stack under the same operating condition. In practice, it is very necessary to clarify the advantage or disadvantage of ASC and CSC, which assists in understanding the effect of cell design on cell performance in the stack level and playing the full potential of the stack by optimizing the cell design.

In literature, there is only one study comparing the performance of the ASC stack with that of the CSC stack under the same operating condition [25]. In that study, the computational domain consists of the fuel and air channels and the electrodes–electrolyte assembly but the ribs are completely ignored. However, many studies have already shown the strong effect of the ribs on the charge and gases transport [13, 26, 27]. For ASC stack, an oxygen depletion zone of 0.46 mm was found with a cathode rib width of only 0.8 mm due to thin cathode thickness limiting the oxygen diffusion to the area under rib [27]. For the CSC stack, the minimum hydrogen concentration under anode rib is only about one third of that under anode channel [28]. Therefore, the model developed in reported [25] can't accurately predict the performance of the ASC or CSC stack.

A 3D model was developed to predict the performance of the ASC or CSC stack. The computational domain comprises the ribs, fuel channels, air channels and the electrodes–electrolyte assembly. Detailed comparisons between ASC stack and CSC stack are made to illustrate the role of the cell design on the stack performance.

2. MODEL

A repeating cell unit of a SOFC stack is shown schematically in Fig. 3a. Due to symmetry, we select half of the repeating unit of stack as our computational domain as shown in Fig. 3b. The computational domain is comprised of (i) cathode-side interconnect plate and the air channels, (ii) electrodes–electrolyte assembly, (iii) anode-side interconnect plate and the fuel channels.

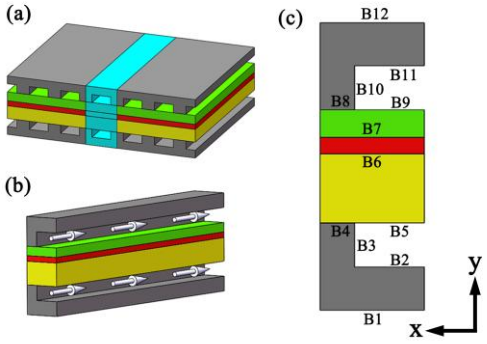

Figure 3. Schematic of a SOFC stack.

2.1. Governing Equations

2.1.1. Charge Transport

Electronic and ionic current density are governed by charge continuity equation, which can be described as follows associated with the point form of Ohm's law.

$$\nabla i_{el} = \nabla(-\sigma_{el}\nabla\varphi_{el}) = 0 \quad (1)$$

$$\nabla i_{io} = \nabla(-\sigma_{io}\nabla\varphi_{io}) = 0 \quad (2)$$

where i_{el} and i_{io} are the electronic and ionic current density, respectively, φ_{el} (φ_{io}) is the local electronic (ionic) potentials, σ_{el} represents the electronic conductivity of electrodes , while σ_{io} represents the ionic conductivity of electrolyte.

The electronic conductivity of composite electrode σ_{el} can be estimated as [29]:

$$\sigma_{el} = \sigma_{el}^{0}[(1-\varepsilon)\phi_{el}\, p_{el}]^{B} \quad (3)$$

where σ_{el}^{0} is the electronic conductivity of the pure material, ε is the porosity, ϕ_{el} is the volume fraction of electronic conductor phase, B is the Bruggeman factor used to include the effects of tortuous conduction paths (B is set as 3.5 [30]) and p_{el} is the probability for electronic conductor particles to belong to the percolated clusters of electronic (ionic) conductor particles.

σ_{el}^{0} for Ni and LSM may be estimated as [26, 31],

$$\sigma_{\mathrm{Ni}}^{0} = 3.27\times10^{6} - 1065.3T \quad (4)$$

$$\sigma_{\mathrm{LSM}}^{0} = \frac{4.2\times10^{7}}{T}\exp\left(\frac{-1150}{T}\right) \quad (5)$$

The ionic conductivity of electrolyte σ_{io} may be estimated as

$$\sigma_{io} = 6.25\times10^{4}\exp(\frac{-10300}{T}) \quad (6)$$

where T is the temperature.

2.1.2. Momentum Transport

Momentum transport in the fuel or air channel can be modeled by applying the Navier–Stokes equation in conjunction with the continuity equation.

$$(\rho u\nabla)u = -\nabla p + \nabla[\mu(\nabla u + (\nabla u)^{T}) - \frac{2}{3}\mu(\nabla u)I] \quad (7)$$

$$\nabla(\rho u) = 0 \quad (8)$$

where ρ is the density, **I** is the identity matrix, μ is the viscosity coefficient of fluid, p is the pressure and u is the velocity of fluid.

2.1.3. Mass Transport

Mass transport mechanism in channel is simple, which can be described by Fick's model associated with the mass continuity equation.

$$\nabla N_i = \nabla(-D_i\nabla C_i + C_i u) = 0 \quad (9)$$

where N_i is the molar flux of species i, C_i is the molar concentration of species i, D_i is the diffusion coefficient of species i, which equates to binary diffusion coefficient D_{ij} due to the fuel compose of two species (H_2, H_2O) and the air compose of two species (O_2, N_2). D_{ij} can be evaluated by following equation.

$$D_{ij} = \frac{3.198\times10^{-8}T^{1.75}}{p\left(v_i^{1/3} + v_j^{1/3}\right)^2}\left(\frac{1}{M_i} + \frac{1}{M_j}\right)^{0.5} \quad (10)$$

where v_i is diffusion volume for specie i (6.12×10^{-6}, 13.1×10^{-6}, 16.3×10^{-6} and 18.5×10^{-6} $m^3\,mol^{-1}$ for H_2, H_2O, O_2 and N_2, respectively [32]) and M_i (M_j) denotes molecular mass of species i (j) (kg mol^{-1}).

Mass transport mechanisms in the porous electrodes are complex, molecular diffusion and Knudsen diffusion are taken into account.

$$\nabla N_i = \nabla(-D_i^{eff}\nabla C_i) = 0 \quad (11)$$

where D_i^{eff} is the equivalent diffusion coefficient of species i, which can be written as

$$D_i^{eff} = \frac{D_{ij}^{eff}D_{iKn}^{eff}}{D_{ij}^{eff} + x_i D_{jKn}^{eff} + x_j D_{iKn}^{eff}} \quad (12)$$

where x_i (x_j) is the molar fraction of species i (j), D_{ij}^{eff} and D_{iKn}^{eff} are the effective binary diffusion coefficient and the effective Knudsen diffusion coefficient of species i respectively.

D_{ij}^{eff} and D_{iKn}^{eff} can be evaluated by following equations respectively [29, 33].

$$D_{ij}^{eff} = \frac{\varepsilon}{\tau}D_{ij} \quad (13)$$

$$D_{iKn}^{eff} = \frac{\varepsilon}{\tau}\frac{2}{3} r_g \sqrt{\frac{8RT}{\pi M_i}} \quad (14)$$

where R is the universal gas constant, r_g is the pore radii and τ is the tortuosity factor.

2.1.4. Heat Transport

Temperature is one of the most critical factors, which significantly affects SOFC performance, because many properties of the SOFC components are temperature dependent such as the electrical and ionic conductivity, the electrochemical reaction rate, fluid properties. For a 3D model, it is essential to take into account heat transport.

In the fluid domain, heat conduction and heat convection are must considered together.

$$\nabla N_T = \nabla(-\lambda_f \nabla T + C_f C_p T u) = 0 \quad (15)$$

where λ_f is the thermal conductivity of the fluid, N_T is the heat flux, C_f is the molar concentration of the fluid, C_p is the molar heat capacity of the fluid, which can be written as [32]

$$C_p = \sum_i x_i C_p^i \quad (16)$$

where C_p^i is the specific heat of species i, which can be calculated as [32]

$$C_p^i = a_i^1 + a_i^2 \times 10^3 T + a_i^3 \times 10^6 T^2 \quad (17)$$

where a_i^1, a_i^2 and a_i^3 are constants.

In the solid domain, heat conduction is considered, which can be described as

$$\nabla N_T = \nabla(-\lambda_s \nabla T) = Q \quad (18)$$

where Q is the heat source, λ_s is the thermal conductivity of the solid.

Heat source Q in SOFC can be classified as Ohmic heat source Q_{ohm}, activation heat source Q_{act} and entropy heat source Q_{entr}.

Q_{ohm} is the heat generation from ohmic loss, which can be expressed as

$$Q_{ohm} = \frac{i^2}{\sigma} \quad (19)$$

Q_{act} is the heat generation from activation loss, which can be expressed as

$$Q_{act} = i\ \eta_{act} \quad (20)$$

Q_{entr} is the heat generation from entropy change in the electrochemical reactions, which can be expressed as

$$Q_{entr} = i\ (-\frac{T\Delta S}{2F}) \quad (21)$$

where F is the Faraday constant, η_{act} is the activation loss and *S* is the entropy.

2.2. Boundary Conditions

As described above, the charge transport equation, momentum transport equation, mass transport equation and heat transport are taken into account in this model. Boundary conditions are

required for solving these coupled partial differential equations. For easy description of boundary conditions, some boundaries in our model are tagged as indicated in Fig. 3c. Many researchers didn't give each of boundaries setting due to so many boundaries in 3D model, which may lead to some misunderstanding. So in this work we describe the boundary setting for each boundary of each equation in order to be easy understanding. Co-flow pattern is adopted in this study, since it has the most uniform temperature distribution than counter-flow pattern or cross-flow pattern [5].

2.2.1. Boundary Setting for the Charge Transport Equation

The boundaries B1 and B12 are the top surface and the bottom surface of half unit cell, respectively, where electronic potential is set as *E* at boundary B1 and φ_{op} is specified at boundary B12. The Nernst potential *E* is given as

$$E = -\frac{\Delta G^0(T)}{2F} + \frac{RT}{2F}\ln\left(\frac{p^0_{H_2}}{p^0_{H_2O}}\left(\frac{p^0_{O_2}}{10^5}\right)^{0.5}\right) \tag{22}$$

where ΔG^0 is the Gibbs free energy change at the condition that the partial pressure of H_2, H_2O and O_2 are all 1 bar. The boundaries B4 and B8 represent the interfaces between rib and electrode. Contact resistance is specified at these boundaries, which means the local current densities cross boundary B4 ($i_{rib\to An}$) and boundary B8 ($i_{Ca\to rib}$) are determined by below expression.

$$i_{rib\to An} = \frac{\varphi_{\mathrm{e,rib/An}} - \varphi_{\mathrm{e,An/rib}}}{ASR_{\mathrm{contact}}} \tag{23}$$

$$i_{Ca\to rib} = \frac{\varphi_{\mathrm{e,Ca/rib}} - \varphi_{\mathrm{e,rib/Ca}}}{ASR_{\mathrm{contact}}} \tag{24}$$

where ASR_{contact} is the contact resistance, $\varphi_{\mathrm{e,rib/An}}$ and $\varphi_{\mathrm{e,An/rib}}$ are the electric potentials at B4 on rib side and anode side, respectively. $\varphi_{\mathrm{e,Ca/rib}}$ and $\varphi_{\mathrm{e,rib/Ca}}$ are the electric potentials at B8 on cathode side and rib side, respectively. The interface between electrolyte and anode is represented by B6, where the normal electronic current density is $-i^{an}_{trans}$ due to the reaction at B6 and the normal ionic current density is i^{an}_{trans}. The interface between electrolyte and cathode is represented by B7, where the normal electronic current density is i^{ca}_{trans} due to the reaction at B7 and the normal ionic current density is $-i^{ca}_{trans}$. All others boundaries are set as electric insulation.

i^{an}_{trans} and i^{ca}_{trans} can be calculated by Butler-Volmer equations as follows [34, 35]:

$$i^{an}_{trans} = i^{\mathrm{an}}_{\mathrm{ref}} \exp\left(-\frac{E_{H_2}}{R}\left(\frac{1}{T}-\frac{1}{T_{\mathrm{ref}}}\right)\right)\left(\frac{p^{TPB}_{\mathrm{H_2}}\, p^{TPB}_{\mathrm{H_2O}}}{p^0_{\mathrm{H_2}}\, p^0_{\mathrm{H_2O}}}\right)\left[\exp\left(\frac{2\alpha^{an}_f F}{RT}\eta^{an}_{act}\right) - \exp\left(-\frac{2\beta^{an}_r F}{RT}\eta^{an}_{act}\right)\right] \tag{25}$$

$$i^{ca}_{trans} = i^{ca}_{ref} \exp\left(-\frac{E_{O_2}}{R}\left(\frac{1}{T}-\frac{1}{T_{ref}}\right)\right)\left(\frac{p^{TPB}_{O_2}}{p^0_{O_2}}\right)^{0.25}\left[\exp\left(\frac{2\alpha^{ca}_f F}{RT}\eta^{ca}_{act}\right) - \exp\left(-\frac{2\beta^{ca}_r F}{RT}\eta^{ca}_{act}\right)\right] \tag{26}$$

where α_{f} and β_{r} are the forward and reverse reaction symmetric factor, respectively, $E_{\mathrm{H_2}}$ and $E_{\mathrm{O_2}}$ are the activation energies for the anode and cathode electrochemical reactions, respectively. $p^0_{H_2}$ and $p^0_{H_2O}$ are the partial pressure of H_2 and the partial pressure of H_2O at the fuel channel inlet, respectively, $p^0_{O_2}$ is the partial pressure of O_2 at the air channel inlet, $p^{TPB}_{H_2}$ and $p^{TPB}_{H_2O}$ are the partial pressure of H_2 and the partial pressure of H_2O at the anode three phase boundaries (TPBs), respectively

and $p_{O_2}^{TPB}$ is the partial pressure of O_2 at the cathode TPBs, i_{ref}^{an} and i_{ref}^{ca} are the exchange transfer current density of anode and cathode respectively.

Here η_{act}^{an} and η_{act}^{ca} are the anode and cathode activation loss respectively, defined as

$$\eta_{act}^{an} = \varphi_{el} - \varphi_{io} - \eta_{conc}^{an} = \varphi_{el} - \varphi_{io} - \frac{RT}{2F}\ln(\frac{p_{H_2}^0}{p_{H_2O}^0}\frac{p_{H_2O}^{TPB}}{p_{H_2}^{TPB}}) \quad (27)$$

$$\eta_{act}^{ca} = \varphi_{io} - \varphi_{el} - \eta_{conc}^{ca} = \varphi_{io} - \varphi_{el} - \frac{RT}{4F}\ln(\frac{p_{O_2}^0}{p_{O_2}^{TPB}}) \quad (28)$$

where η_{conc}^{an} (η_{conc}^{ca}) is the anode (cathode) concentration loss.

2.2.2. Boundary Setting for the Mass Transport Equation

At the channel inlets, the concentration of gaseous species are imposed, whereas, the convective fluxes are considered at the channel outlets, which mean diffusive component across the channel outlets is zero. The boundaries B5 and B9 represent the interfaces between channel and electrode, where species fluxes are continuous. As there is electrochemical reaction at boundaries B6 and B7, the normal molar flux of hydrogen, water and oxygen are $i_{trans}^{an}/(2F)$, $-i_{trans}^{an}/(2F)$, $i_{trans}^{ca}/(4F)$, respectively. The insulation condition is set at all other boundaries, which implies the molar flux of species is zero.

2.2.3. Boundary Setting for the Momentum Transport Equation

At the channel inlets, the uniform inlet velocity are applied, whereas, pressure and the normal flow are imposed at the channel outlets. The no slip condition is considered at all others boundaries, which means $u = 0$.

2.2.4. Boundary Setting for the Heat Transport Equation

At the channel inlets, the uniform temperature are applied, whereas, the convective fluxes are considered at the channel outlets. The boundary condition at boundary B4 and B8 become as $\vec{n} \cdot N_T = Q_{ohm}$ due to contact resistance. The boundary condition at boundary B6 and B7 are specified as $\vec{n} \cdot N_T = Q_{act} + Q_{entr}$ due to the reaction. Boundary B2, B3, B10 and B11 are the interfaces between rib and channel, where the convection heat between rib and channel is considered.

For rib, convection heat transfer rate is given as

$$-\vec{n} \cdot N_T = h(T_{chan/rib} - T_{rib/chan}) \quad (29)$$

For fluid in channel, convection heat transfer rate is given as

$$-\vec{n} \cdot N_T = -h(T_{chan/rib} - T_{rib/chan}) \quad (30)$$

where $T_{chan/rib}$ ($T_{rib/chan}$) is the temperature at the interfaces between rib and the channel on channel (rib) side.

Adiabatic boundary condition is employed at all other boundaries since the simulation region is the half of one repeating unit located at the center of stack.

2.3. Numerical Implementation

The model was implemented in the finite element commercial software COMSOL MULTIPHYSICS. The COMSOL stationary nonlinear solver uses an affine invariant form of the damped Newton method to solve the discretized PDEs with a relative convergence tolerance of 1×10^{-6}. The mesh is composed of 6,540 elements with 117,279 degrees of freedom. The values of input parameters for the base case are summarized in Table 1 and Table 2 unless otherwise stated.

Table 1. Model parameters.

Parameter	Value
Fuel channel inlet velocity, u_0^{fuel} (m s^{-1})	0.3
Air channel inlet velocity, u_0^{air} (m s^{-1})	3
Fuel channel outlet pressure, p_0 (Pa)	10^5
Air channel outlet pressure, p_0 (Pa)	10^5
Fuel channel inlet temperature, T_{inlet} (K)	973.15
Air channel inlet temperature, T_{inlet} (K)	973.15
Inlet concentration (mol m^{-3})	
$c^0_{H_2}$	12.147
$c^0_{H_2O}$	0.376
$c^0_{O_2}$	2.63
$c^0_{N_2}$	9.893
Tortuosity factor, τ	3.5
Porosity, ε	0.3
Porous radius, r_g (m)	5e-7
Activation energies for the cathode, E_{O_2} (J mol^{-1})	130×10^3
Reaction symmetric factor for cathode, $\alpha_f^{ca}, \beta_r^{ca}$	0.75, 0.5
Exchange transfer current density of cathode, i_{ref}^{ca} $\left(\text{Am}^{-1}\right)$	4000
Exchange transfer current density of anode, i_{ref}^{an} $\left(\text{A m}^{-1}\right)$	5000
Activation energies for the anode, E_{H_2} (J mol^{-1})	120×10^3
Reaction symmetric factor for anode, $\alpha_f^{an}, \beta_r^{an}$	1, 0.5
Operation voltage, φ_{op} (V)	0.7
Thermal conductivity of anode, λ_{an} (W m^{-2} s^{-1})	2 [36]
Thermal conductivity of electrolyte, λ_{elec} (W m^{-2} s^{-1})	2 [36]

Thermal conductivity of cathode, λ_{ca} (W m^{-2} s^{-1})	4 [36]
Thermal conductivity of rib, λ_{rib} (W m^{-2} s^{-1})	6 [37]
Area specific contact resistance at the rib-electrode interface, $ASR_{contact}$ (Ω cm^2)	0.03
Channel length, L_{ch} (mm)	20
Channel width, w_{ch} (mm)	1.5
Interconnect height, h_{int} (mm)	2.0
Rib width, w_{rib} (mm)	1.5
Rib height, h_{rib} (mm)	1.0

Table 2. Coefficients of molar heat capacity [38]

Gases	a_i^1	$a_i^2 \times 10^3$	$a_i^3 \times 10^6$
Hydrogen	29.09	0.836	-0.3265
Water	30	10.7	-2.022
Oxygen	36.16	0.845	-0.7494
Nitrogen	27.32	6.226	-0.9502

3. RESULTS AND DISCUSSION

In order to investigate the performance discrepancy between the ASC stack and the CSC stack, two models were established with the same settings as described above except the thickness of electrodes. The ASC stack model has an anode thickness and a cathode thickness of 500 and 50μm, respectively. The corresponding parameters for the CSC stack model are 50 and 500μm, respectively. It is some unexpected to find that the average current density of the ASC stack is only 5580 A m^{-2}, a reduction of 20.7% from the CSC stack of 7033 A m^{-2}. The substantial discrepancy between the performances of the ASC stack and the CSC stack may be understood by the difference distributions of gases concentration and electronic potential in Fig. 4-5.

3.1 The Distributions of Gases Concentration

Fig. 4 illustrates the oxygen concentration distribution in the air channel and cathode of the ASC stack and the CSC stack. For the ASC stack, the oxygen concentration in the vertical electrode surface direction is almost uniform, which benefits from thin cathode. However, on the other hand, the thin cathode simultaneously also limits the oxygen diffusion to the area under rib and leads to a wide oxygen depletion zone under the rib, as shown in Fig. 4a. As a result, electrochemical reaction can't take place in oxygen depletion zone due to the lack of the oxygen. For the CSC stack, cathode is the thickest layer. Thick cathode provides a wide alleyway allowing oxygen to penetrate under the ribs.

Although the oxygen concentration of the CSC stack under rib is small, an oxygen depletion zone is avoided, as can be seen in Fig. 4b. Thus, the effective reaction zone of the CSC stack is larger than that of the ASC stack, which is an important factor contributing to the reduced performance of the ASC stack.

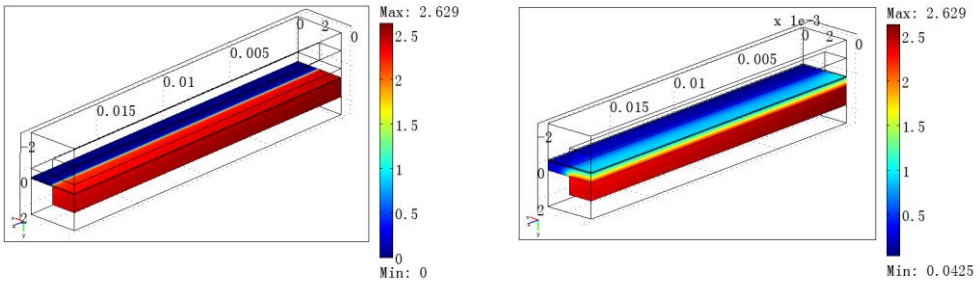

(a) (b)

Figure 4. Distributions of O_2 for (a) the ASC stack and (b) the CSC stack

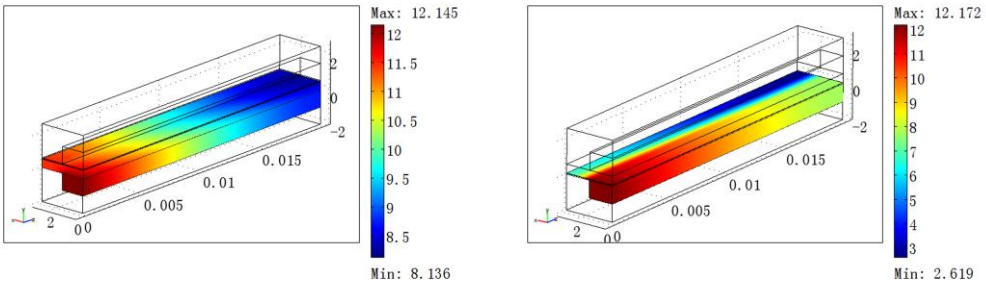

(a) (b)

Figure 5. Distribution of H_2 for (a) the ASC stack and (b) the CSC stack

Fig. 5 provides the hydrogen concentration in the fuel channel and anode of the ASC stack and the CSC stack. As expected, the highest value of hydrogen concentration is located at the channel inlet, while a progressive hydrogen concentration decrease is observed moving to the cell outlet. Comparing Fig. 5a and 5b, it is obvious that the hydrogen concentration distribution along fuel flow direction under channel for the ASC stack is similar to that for the CSC stack at the corresponding position. For the ASC stack, the hydrogen concentration under rib is almost as big as that under channel, as shown in Fig. 5a. While Fig. 5b shows a quite different situation. There is a large hydrogen concentration gradient in the x direction for the CSC stack. Although hydrogen concentration of the ASC stack under rib is bigger than that of the CSC stack at the corresponding position, the most hydrogen under rib of the ASC stack doesn't take part in the electrochemical reaction because of a wide oxygen depletion zone under rib, as shown in Fig. 4a.

3.2 The Distributions of Electronic Potential

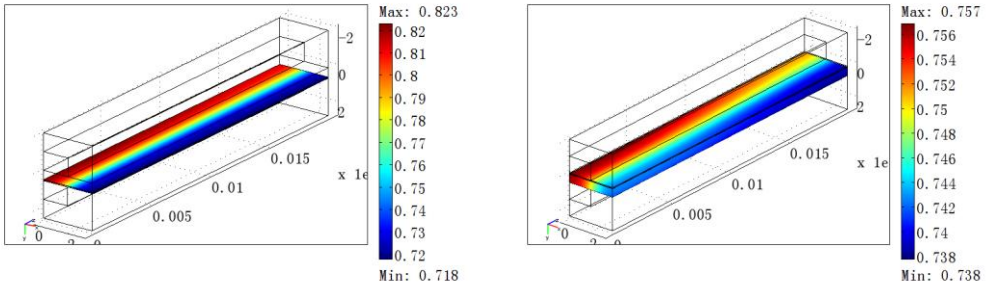

(a) (b)

Figure 6. Distribution of electronic potential in cathode for (a) the ASC stack and (b) the CSC stack

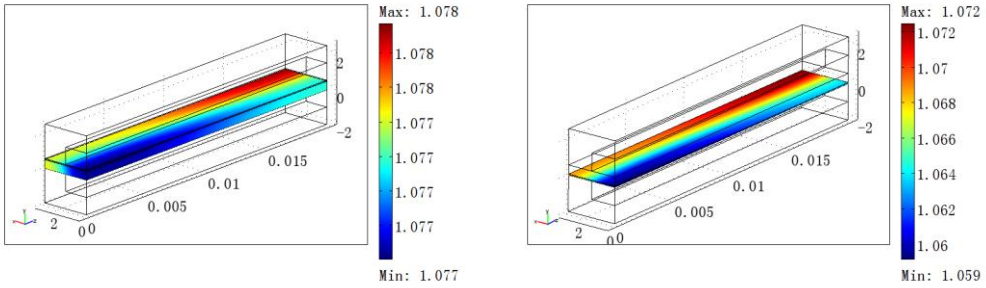

(a) (b)

Figure 7. Distribution of electronic potential in anode for (a) the ASC stack and (b) the CSC stack

The distribution of electronic potential in cathode for the ASC stack and the CSC stack is given in Fig. 6. The ohmic loss in cathode for the CSC stack is 19 mV, which is less than one fifth of that for the ASC stack (105 mV). Notable cathode ohmic loss of the ASC stack is created by two main aspects: (i) a narrow cross-section of current path in the x direction (ii) relatively small cathode electrical conductivity. A very small electronic potential variation is observed in anode for the ASC stack, as shown in Fig. 7a. The high anode electrical conductivity is believed to be responsible. For the CSC stack, the ohmic loss in anode is about 13 mV, as given in Fig. 6b. Large anode ohmic loss of the CSC stack is attributed to thin anode hindering current flow in the x direction. The total electrodes ohmic loss for the CSC stack is 32 mV, which is only about one third of that for the ASC stack 106 mV. This is another factor contributing to the reduced performance of the ASC.

3.3 The Distributions of temperature

Fig. 8 shows the distribution of temperature in the ASC stack and the CSC stack. It is evident that for the ASC stack, temperature is increase along the direction of fuel flow and the lowest temperature is located at the input of channel. Similar situation can be found in the CSC stack.

However, the highest of the CSC stack is 1027 K is larger than that of the ASC stack. Compared with the CSC stack, as described above, the performance of the ASC is lower. As a result, the heat produced by reaction is also lower. Temperature is one of the most critical factors, since the stack performance rises quickly with increasing temperature. If temperature is not considered, the advantage of the CSC stack will be underestimated.

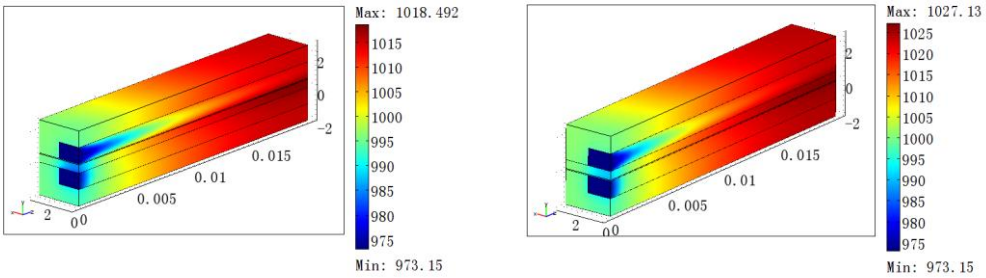

Figure 8. Distribution of temperature for (a) the ASC stack and (b) the CSC stack

3.4 Effect of Rib Width

To gain more insight into the performance difference between the ASC stack and the CSC stack, the stack output for a fixed pitch width (the sum of the rib and the channel width) of 3 mm is examined by varying the rib width.

Fig. 9a shows the relationship between the output current density and the anode rib width. The output current density of the ASC stack and CSC stack for a fixed rib width of 1.5 mm are respectively 5580 and 7033 A m^2, which are 6.4% and 23.5% higher than that of the ASC stack and CSC stack with an anode rib width of 2.1 mm, respectively. Clearly, the anode rib width has a significant impact on the performance of the ASC stack and the CSC stack. Similarly, the cell outputs of the ASC stack and CSC stack also vary notably with the cathode rib width, as shown in Fig. 9b. Compared to the results obtained with a fixed cathode rib width of 2.1 mm, the output current increases by 12.4% and 27.3% for the ASC stack and the CSC stack respectively with a cathode rib width set as 1.5 mm. Therefore, a suitable choice of the rib width is very important for realizing the potential of a SOFC stack.

On the other hand, the performance difference between the ASC stack and the CSC stack depends strongly on the rib width. It is evident that the maximum current density of the CSC stack is larger than that of the ASC stack, as given in Fig. 9a and 9b. However, the advantage associated with the CSC stack may be greatly reduced, or even lost completely, if the rib width is not chosen appropriately. For example, for a fixed anode rib width of 2.4 mm, the output current densities of the CSC stack is less than that of the ASC stack.

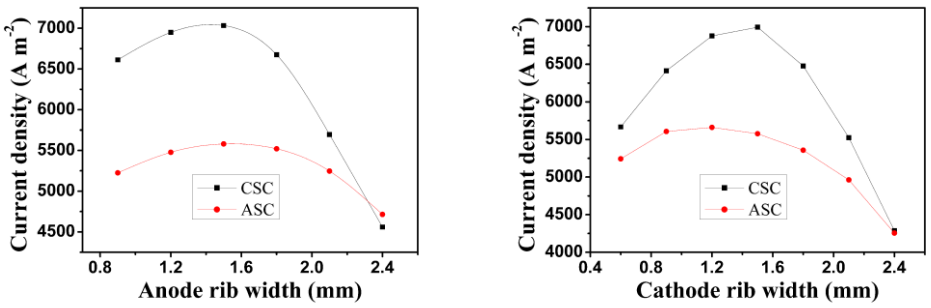

(a) (b)

Figure 9. The effect of rib width on the stack output current density (a) anode rib width and (b) cathode rib width

3.5 Effect of Contact Resistance and Pitch Width

As discussed above, the stack performance is closely related to the anode and cathode rib width. Thus, the optimal rib width is used in the following, which can be obtained according to the optimal rib width formulae presented in references [13, 39].

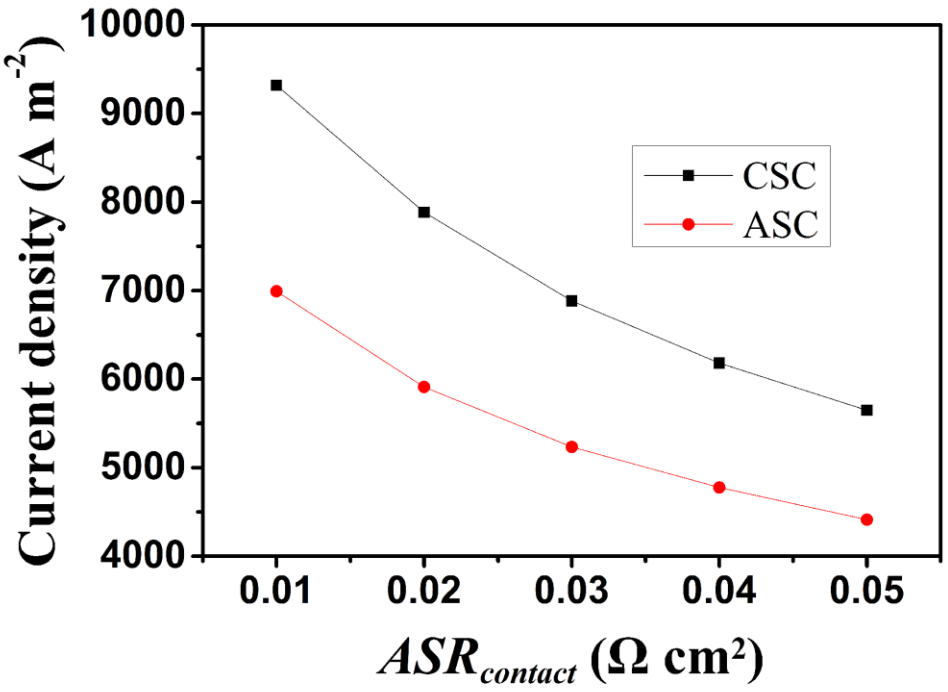

Figure 10. The effect of $ASR_{contact}$ on the stack output current density

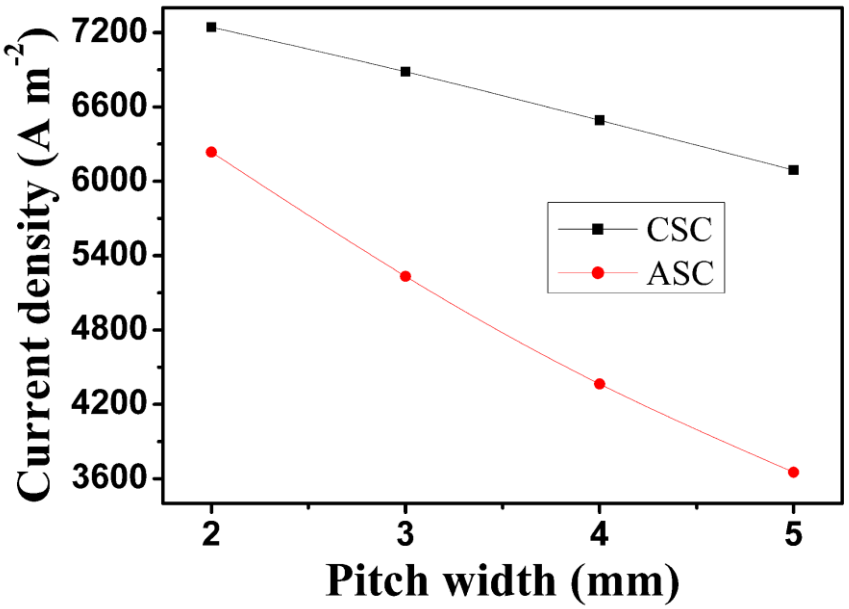

Figure 11. The effect of pitch width on the stack output current density

Fig. 10 depicts the dependence of $ASR_{contact}$ on the stack output current density. Obviously, the performance of the CSC is much better than that of the ASC for any practical $ASR_{contact}$. As expect, the output current density of the ASC stack and CSC stack decreases with the increase of the contact resistance ($ASR_{contact}$), as can be seen in Fig. 10. However, it is surprise that $ASR_{contact}$ has so significant influence on SOFC performance. The output current density increases 40% and 34% from $ASR_{contact}$ =0.05Ω/cm^2 to $ASR_{contact}$ =0.02Ω/cm^2 for the CSC stack and ASC stack respectively. As a consequence, it is rather necessary to minimize $ASR_{contact}$ for the improving SOFC performance.

As depicted in Fig. 11, with the increase of the pitch width, the advantage of the CSC stack over the ASC stack becomes more and more obvious. The output current densities of the CSC stack and the ASC stack decrease by 16% and 41% for the pitch width varying from 2 to 5 mm respectively. The performance reduction is mainly due to two aspects: (i) the increase of the gases transport path in the parallel electrode surface direction leading to larger concentration overpotential, as the optimal rib width is proportional to the pitch width. (ii) the increased ohmic overpotential for the increased charge transport route in the parallel electrode surface direction due to the wider channel associated with the wider pitch.

4. CONCLUSIONS

A 3D mathematic model has been developed to illustrate the effect of cell design on SOFC stack performance and to understand the underlying mechanism. The gas concentration, electrical potential distribution and temperature distribution are compared between the ASC stack and the CSC

stack. Moreover, the discrepancy between the ASC stack and the CSC stack are examined by varying rib width, contact resistance and pitch width. The conclusions are summarized as follows:

1) The performance of ASC stack is considerably lower than the CSC stack, which is mainly due to two aspects: (i) a wide oxygen depletion zone under rib limits the effective reaction zone of the ASC; (ii) thin cathode of the ASC leads to remarkable cathode ohmic loss;

2) With the optimal rib width, the performance of the CSC stack is better than that of the ASC stack for any practical contact resistance. However, it is possible that the ASC stack is superior to the CSC, if the rib width is not chosen appropriately.

3) It is rather necessary to minimize contact resistance ($ASR_{contact}$) for the improvement of the SOFC performance. The output current density increases 40% and 34% from $ASR_{contact}$ =0.05Ω/cm^2 to $ASR_{contact}$ =0.02Ω/cm^2 for the CSC and ASC.

4) Although the performance of the CSC stack and the ASC stack decrease with the increase of the pitch width, the advantage of the CSC stack over the ASC stack becomes more and more obvious.

The present study signifies the differences between the ASC stack and CSC stack and provides better understanding on the effect of cell design on SOFC stack performance.

ACKNOWLEDGEMENTS

We gratefully acknowledge the financial support of the National Science Foundation of China (21406095 and 21106058), the Jiangsu Province Colleges and Universities Natural Science Projects (13KJB480003) and the Jiangsu University of Science and Technology (35321101). The authors thank Dr. Shixue Liu at Kyushu University for his insightful discussions.

References

1. M. M. Hussain, X. Li, I. Dincer, *Journal of Power Sources*,189(2009), 916-28.
2. A. V. Virkar, J. Chen, C. W. Tanner, J-W. Kim, *Solid State Ionics*,131(2000),189-98.
3. Y. Ji, K. Yuan, J.N. Chung, Y.C. Chen, *Journal of Power Sources*,161(2006), 380-91.
4. L. W. Chen, S. H. Gao, H. C. Zhang, *International Journal of Electrochemical Science*, 8 (2013), 10772 -10787.
5. J. H. Myung, H. J. Ko, J. J. Lee, S. H. Hyun, *International Journal of Electrochemical Science*, 6 (2011) , 1617-1629.
6. S. Zhang, L. Bi, L. Zhang, C. Yang, H. Wang, W. Liu, *International Journal of Hydrogen Energy*,34(2009), 7789-94.
7. M. Ni, *International Journal of Hydrogen Energy*, 37(2012), 1731-45.
8. Z. Zhao, L. Liu, X. Zhang, W. Wu, B. Tu, D. Cui, et al. *International Journal of Hydrogen Energy*, 38(2013),15361-70.
9. F. Miao, *International Journal of Electrochemical Science*, 8 (2013) , 11814-11822.
10. H. C. Patel, N. Biradar, V. Venkataraman, P. V. Aravind, *International Journal of Electrochemical Science*, 9(2014) , 4048-4053.
11. Y. Wang, J. Yu, S. Weng, *International Journal of Hydrogen Energy*, 36(2011), 5624-31.
12. H. S. Noh, J. Hwang, K. Yoon, B. K. Kim, H. W. Lee, J. H. Lee, et al, *Journal of Power Sources*, 230(2012), 109-14.
13. W. Kong, J. Li, S. Liu, Z. Lin , *Journal of Power Sources* ,204(2012), 106-15.
14. Y. M. Park, H. J. Lee, H. Y. Bae, J. S. Ahn, H. Kim , *International Journal of Hydrogen Energy*, 37(2012),4394-400.

15. H. T. Lim, S. Hwang, M. Jung, H. Park, M. Park, S. S. Lee, et al, *Fuel Cells*,13(2013), 712-9.
16. G. Chen, G. Guan, Y. Kasai, H. X. You, A. Abudula, *Journal of Solid State Electrochemistry*, 16(2012)2071-7.
17. G. Chen, H. X. You, Y. Kasai, H. Sato, A. Abudula, *Journal of Alloys and Compounds*, 509(2011), 5159-62.
18. M. Liu, D. Dong, F. Zhao, J. Gao, D. Ding, X. Liu, et al, *Journal of Power Sources*,182(2008), 585-8.
19. G. Chen, G. Guan, Y. Kasai, A. Abudula, *International Journal of Hydrogen Energy*, 37(2012), 477-83.
20. M. A. Khan, R. Raza, R. B. Lima, M. A. Chaudhry, E. Ahmed, G. Abbas, *International Journal of Hydrogen Energy*, 38(2013), 16524-31.
21. D. Cui, C. Yang, K. Huang, F. Chen, *International Journal of Hydrogen Energy*, 35(2010), 10495-504.
22. S.H. Chan, K.A. Khor, Z.T. Xia, *Journal of Power Sources*, 93(2001), 130-40.
23. S. Q. Yang, T. Chen, Y. Wang, Z. Peng, W. G. Wang, *International Journal of Electrochemical Science*, 8(2013), 2330-44.
24. M. Kornely, A. Leonide, A. Weber, E. Ivers-Tiffée, *Journal of Power Sources*, 196(2011), 7209-16.
25. T. X. Ho, P. Kosinski, A. C. Hoffmann, A. Vik ,*Chemical Engineering Science*, 64(2009), 3000-9.
26. D. H. Jeon, J. H. Nam, CJ. Kim, *Journal of the Electrochemical Society*, 153(2006), A406-A17.
27. S. Liu, C. Song, Z. Lin, Journal of Power Sources, 183(2008), 214-25.
28. W. Kong, S. C. Su, X. Gao, D. H. Zhang, Z. D. Yu, *Advanced Materials Research*, 712(2013), 1325-9.
29. J. H. Nam, D. H. Jeon, *Electrochim Acta*, 51(2006), 3446-60.
30. J. Sanyal, G. M. Goldin, H. Zhu, R. J. Kee, *Journal of Power Sources*, 195(2010), 6671-9.
31. Y. X. Shi, N. S. Cai, C. Li, *Journal of Power Sources*, 164(2007), 639-48.
32. B. Todd, J. B.Young, *Journal of Power Sources*, 110(2002), 186-200.
33. E. Fuller, P. Schettler, J. Giddings, *Industrial & Engineering Chemistry*, 58(1966), 18-27.
34. P. Costamagna, K. Honegger, *Journal of the Electrochemical Society*, 145(1998), 3995-4007.
35. H. Y. Zhu, R. J. Kee, *Journal of the Electrochemical Society*, 155(2008), B715-B29.
36. L. Petruzzi, S. Cocchi, F. Fineschi, *Journal of Power Sources*, 118(2003), 96-107.
37. M. Iwata, T. Hikosaka, M. Morita, T. Iwanari, et al, *Solid State Ionics*, 132(2000), 297-308.
38. F. P. Incropera, D. P. Dewitt, T. L., *Bergman & Llavine AS*, 2007, 572-5.
39. W. Kong, X. Gao, S. X. Liu, S. C. Su, D. F. Chen, *Energies*, 7(2014), 295-313.